Molecular dynamics simulation of Fe-Si alloys using a neural network machine learning potential

Huaijun Sun,[1,2] Chao Zhang,[3] Ling Tang,[4] Renhai Wang,[5] Weiyi Xia,[2,6] and Cai-Zhuang Wang[2,6,*]

[1]*Jiyang College of Zhejiang Agriculture and Forestry, University, Zhuji 311800, China*
[2]*Ames Laboratory, U.S. Department of Energy, Ames, Iowa 50011, USA*
[3]*Department of Physics, Yantai University, Yantai 264005, China*
[4]*Department of Applied Physics, College of Science, Zhejiang University of Technology, Hangzhou 310023, China*
[5]*School of Physics and Optoelectronic Engineering, Guangdong University of Technology, Guangzhou 510006, China*
[6]*Department of Physics and Astronomy, Iowa State University, Ames, Iowa 50011, USA*

(Received 4 December 2022; accepted 17 May 2023; published 2 June 2023)

Interatomic potential development using machine learning (ML) approaches has attracted a lot of attention in recent years because these potentials can effectively describe the structural and dynamical properties of complex materials at the atomistic level. In this work, we present the development of a neural network (NN) deep ML interatomic potential for Fe-Si alloys, and we demonstrate the effectiveness of the NN-ML potential in predicting the structures and energies of liquid and crystalline phases of Fe-Si alloys in comparison with the results from *ab initio* molecular dynamics simulations or experimental data. The developed NN-ML potential is also used to perform molecular dynamics simulations to study the structures of Fe-Si alloys with various compositions under rapid solidification conditions. The short-ranged orders in the rapidly solidified Fe-Si alloys are also analyzed by a cluster alignment method.

DOI: 10.1103/PhysRevB.107.224301

I. INTRODUCTION

In addition to high academic research interest, Fe-Si alloys have great potential in advanced technological applications due to their various unique physical properties [1]. A crystalline Fe_3Si alloy with DO_3 structure is a metallic ferromagnet at room temperature, and it can be used as an efficient spin-injection source in magnetic devices [2,3]. The cubic ε-FeSi compound is a semiconductor with unusual magnetic properties [1,4], while the β-$FeSi_2$ alloy with a band gap of about 0.87 eV is expected to be applied in air atmosphere at high temperature as an excellent thermoelectric material [5,6]. Moreover, Fe-Si alloys are often used as initial materials for commercial alloys with complex components such as Sendust alloy (Fe-Si-Al) [7,8] and Finement (Fe-Si-B-Cu-Nb) [9–11]. In addition to the crystalline phases, amorphous Fe-Si alloys have also attracted considerable interest [3,12–16]. Several Fe-Si amorphous alloys have also been made by experiments [3,12–16]. It has been shown that structural disordering is an important means to tune the electronic and magnetic properties of Fe-Si alloys [3]. For the Fe-rich amorphous Fe-Si alloys, the spin polarization has been confirmed to be larger than the corresponding value in the ordered phase [12], which can be designed as amorphous spintronic material. On the Si-rich side, amorphous Fe-Si alloys have been reported to possess a similar band gap to that of crystalline structures, but they exhibit a larger optical absorption coefficient [13–16], which is suitable for use in optoelectronic technologies. Therefore, understanding the structures of amorphous Fe-Si alloys with different composition ratios is essential for elucidating the properties and functionalities observed.

The energetic stability, physical properties, and local chemical order of Fe-Si alloys have been investigated extensively in the past several decades by both experimental and theoretical studies [17–21]. So far, the *ab initio* molecular dynamics (AIMD) method based on the first-principles density functional theory (DFT) has been widely used. AIMD can accurately describe the interatomic interactions and total energies for different Fe-Si structures, and it has demonstrated good agreement with available experimental data [22,23]. However, most of AIMD can only be performed for a short time (less than 1 ns) and several hundred atoms because of the expensive computational cost. Therefore, it is difficult for AIMD to investigate the phase-competition during solidification and long-time relaxation in amorphous structures [24].

To overcome these limitations in AIMD, some empirical interatomic potentials, such as Lennard-Jones [25], the embedded-atom method (EAM) [26,27], and Tersoff and Stillinger-Weber potentials [28–30], have been developed. These potentials have been very useful in MD simulation studies of some classes of materials [31,32]. Among them, the EAM potentials can give a good description for metallic systems [27,33]. However, due to the different bonding features, it is still difficult to get a suitable EAM potential to describe the atomistic behaviors for complex materials containing different types of bonding, such as the Fe-Si system with mixed metallic and covalent bonds [33–35].

Recently, it has been shown that accurate interatomic potentials can be generated for reliable MD simulations by using deep machine learning based on artificial neural networks. In particular, the deep potential molecular dynamics (DeepMD), a neural network learning software package, has been developed which can accurately describe the interatomic interactions in complex materials involving various bonding

*wangcz@ameslab.gov

TABLE I. A list of liquid training data sets.

System	Number of atoms	Temperatures (K)	Simulation time (ps)	Number of snapshots
$Fe_{10}Si_{90}$ liquid	128	1600,1700,1800,1900,2000	60 for each temperature	108000
$Fe_{11}Si_5$ liquid	128	1600,1700,1800,1900,2000	60 for each temperature	214000
FeSi liquid	128	1600,1700,1800,1900,2000	60 for each temperature	332000
Fe liquid	250	1600,1700,1800,1900,2000	60 for each temperature	28000
Si liquid	256	1600,1700,1800,1900,2000	60 for each temperature	106000

environments [36–39]. Neural network machine learning (NN-ML) potentials developed from DeepMD have been demonstrated to be accurate in predicting the structural and dynamical properties of alloy materials [24,35–37]. Moreover, while the accuracy of NN-ML potentials obtained from DeepMD is close to that of DFT calculation, MD simulations using NN-ML potentials are much faster than AIMD simulations [40,41]. For a system with 5000 atoms, MD simulations using NN-ML potentials can be about 10^6 times faster than AIMD [24,37,42]. Therefore, the development of NN-ML potentials opens the door to performing accurate and reliable MD simulations for a larger size and a longer simulation time.

In this paper, by using the DeepMD method, we develop a NN-ML interatomic potential for Fe-Si alloys. By comparing with first-principles DFT calculations, we show that the developed NN-ML potential describes well the liquid states of Fe-Si alloys with compositions $Fe_{11}Si_5$, FeSi, and $Fe_{10}Si_{90}$, respectively. The NN-ML potential also accurately described the energy versus volume curves for a number of crystalline structures, including Fe_2Si, Fe_5Si_3, FeSi, $Fe_{11}Si_5$, Fe_3Si, and $FeSi_2$. The NN-ML potential is then used to study the rapid solidification of $Fe_{11}Si_5$, FeSi, $Fe_{30}Si_{70}$, $Fe_{20}Si_{80}$, and $Fe_{10}Si_{90}$ by MD simulations. We found that under a cooling rate of 10^{11} K/s, all Fe-Si liquid alloys are developed into an amorphous state except for $Fe_{10}Si_{90}$, in which partial crystallization has been observed. Using the cluster alignment method, the short-ranged orders (SRO) in the quenched Fe-Si alloy samples at 300 K obtained from the MD simulations are analyzed and classified.

The rest of the paper is organized as follows. In Sec. II, data preparation and ML training for the NN-ML potentials is described. In Sec. III, the accuracy of the developed NN-ML potentials for liquid and crystalline Fe-Si alloys is demonstrated in comparison with the first-principles DFT results or experimental data. The structures of Fe-Si alloys (including the SRO analysis) with various compositions under rapid solidification by MD simulations are presented in Sec. IV, followed by a summary in Sec. V.

II. DATA PREPARATION AND DEEPMD TRAINING

The data used in training the NN-ML potential by DeepMD contain snapshots from the liquids of pure Fe and Si as well as $Fe_{11}Si_5$, FeSi, and $Fe_{10}Si_{90}$ alloys at different temperatures, in addition to various crystalline phases of pure Fe, pure Si, and Fe-Si binary compounds with random displacements imposed.

First-principles DFT calculations for the crystalline structures are performed using the Vienna ab initio simulation package (VASP) [43,44]. The projector augment wave (PAW) method [45] is adopted for describing the interaction between core-valence electrons. The electron exchange and correlation potential are determined by the generalized gradient approximation (GGA) in the Perdew-Burke-Ernzerhof (PBE) formula [46]. The kinetic energy cutoff of 520 eV for the plane-wave basis set is chosen, and the Monkhorst-Pack k mesh with $2\pi \times 0.03\,\text{Å}^{-1}$ spacing is utilized to sample the Brillouin zone. The electronic convergence criteria of energies and forces are set to 10^{-5} eV/atom and 0.01 eV/Å, respectively, for the relaxation of the unit-cell lattice vectors.

The crystalline phases include body-centered-cubic, face-centered-cubic, and hexagonal Fe structures, and crystalline Si with cubic diamond structure ($Fd3m$), hexagonal diamond structure ($P6_3/mmc$), orthorhombic structure ($Cmcm$), and BC structure ($R3$), as well as the binary Fe_2Si, Fe_5Si_3, FeSi, $Fe_{11}Si_5$, Fe_3Si, and $FeSi_2$ line compounds, are obtained from the Materials Project (MP) database [47]. The unit cell is contracted or expanded by a scaling factor ranging from 0.85 to 1.225 with 0.025 intervals for each Fe-Si crystal structure, and from 0.85 to 1.245 with 0.005 intervals for Fe and Si crystal structures. For each given volume, the atoms in the crystal are randomly displaced from their equilibrated position with a distortion amplitude between −0.025 and 0.025 of the length of the lattice vectors. Fifty distorted structures are randomly generated for each crystalline phase. Then, single-point DFT calculations are performed for these structures to obtain the energies and forces (on each atom). These calculation results are also collected into the training database. All training data used in the present paper are listed in Tables I and II.

TABLE II. A list of crystal training data sets.

System	Space group	Number of atoms	Number of distorted structures
$FeSi_2$	$P4/mmm$	3	800
Fe_2Si	$P3m1$	6	800
Fe_5Si_3	$P6_3/mcm$	16	800
FeSi	$P2\_13$	8	800
$Fe_{11}Si_5$	$Pm3m$	16	800
Fe_3Si	$Fm3m$	16	800
$FeSi_2$	$Cmce$	48	800
Fe	$P6_3/mmc$	2	4000
Fe	$Fm3m$	4	4000
Fe	$Im3m$	2	4000
Si	$R3$	24	4000
Si	$P6_3/mmc$	4	4000
Si	$Ia3$	16	4000
Si	$Fd3m$	4	4000
Si	$Cmcm$	24	4000

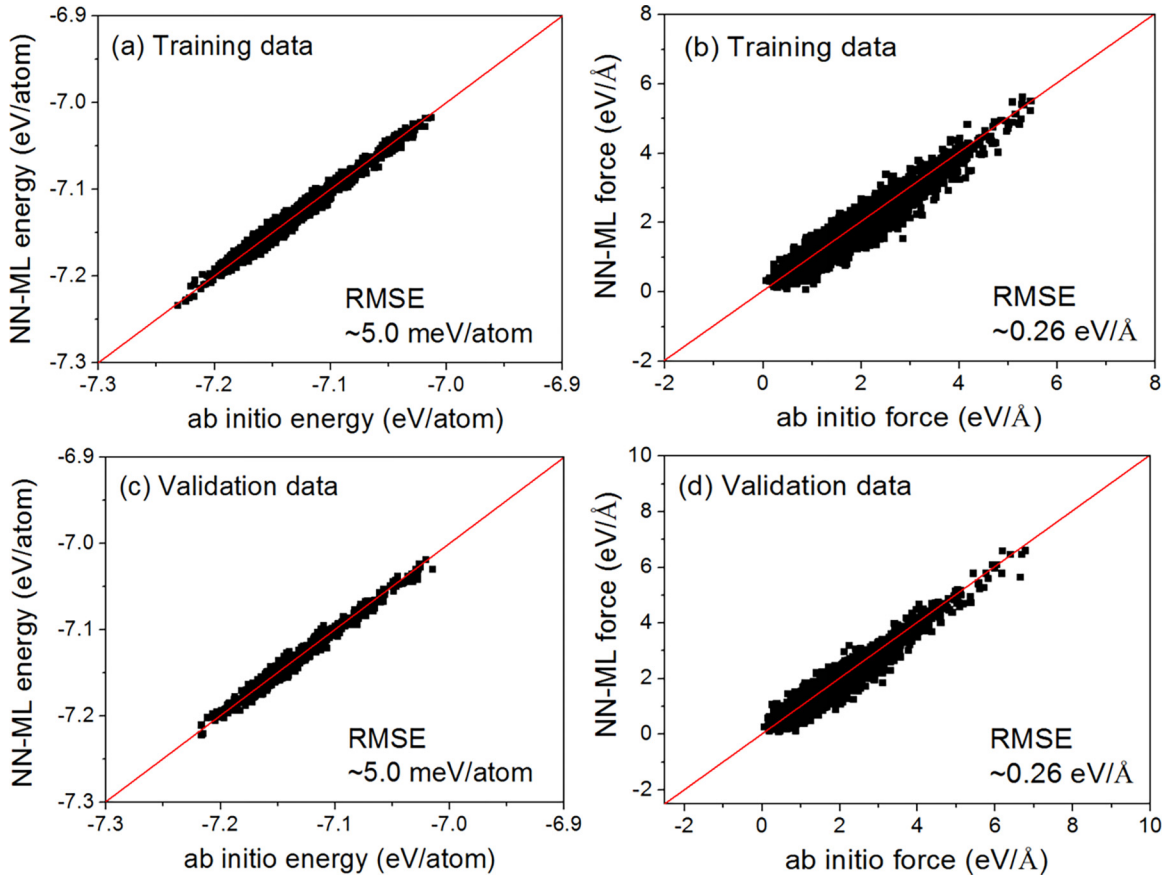

FIG. 1. The comparison of the energies and the magnitude of forces predicted by the trained NN-ML model and *ab initio* calculation results for the training and validation data of $Fe_{11}Si_5$ liquid structure.

For generating the liquid snapshots training data, AIMD simulations are also carried out using VASP with a constant number of atoms, constant volume, and temperature (*NVT*) ensemble using a Nosé-Hoover thermostat under periodic boundary conditions and a MD time step of 3 fs [48]. The simulation temperatures for pure Fe and Si liquids and three liquid alloys, i.e., $Fe_{11}Si_5$, FeSi, and $Fe_{10}Si_{90}$, are at 2000, 1900, 1700, and 1600 K separately. For each simulation temperature, the MD box size is constantly adjusted so that the average pressure of the system is in the range of $-10.0 - 10.0$ Kbar. The numbers of snapshots for the liquids at different compositions are picked up somewhat randomly. We collected these snapshot structures together with their potential energies and forces on each atom from the AIMD simulations, and we used them as the training data.

The DeepPot-SE model as implemented in the DeepMD-Kit package [49] is used to train the NN-ML potential. The radial cutoff of the model is taken as 7.0 Å for capturing the neighbor configuration information around each atom, and the smooth cutoff radius is set as 6.8 Å. The filter net has two hidden layers with 60 and 120 neurons, respectively, and the fitting net has three hidden layers with 240 neurons for each layer. The data set from DFT calculations and AIMD simulations is randomly divided into 97% and 3% of training and validation set, respectively. The learning rate decreases exponentially with the decay rate of 0.96 every 10 000 steps. The initial learning rate is set as 0.001. To achieve a satisfied accuracy, a total of 3 000 000 steps are performed for the training process. In Fig. 1, we compare the results of the energies and forces from our NN-ML prediction for the $Fe_{11}Si_5$ liquid structure with those from DFT calculations. The energies and forces predicted by our NN-ML potential agree very well with DFT calculations, and most of the data points are concentrated near the perfect-fit line with a small root-mean-square errors (RMSE) of 5.0 meV/atom and 0.26 eV/Å for the energy and the magnitude of forces, respectively. Moreover, the comparison of energies and forces for the $Fe_{30}Si_{70}$ alloy, which is not included in the training dataset, also shows a good agreement between our NN-ML potential results and DFT data, as can be seen from Fig. 2. These results indicate that the training accuracy from the DeepMD is satisfactory, and no sign of overfitting is observed.

III. PERFORMANCE OF THE NN-ML POTENTIAL FOR Fe-Si ALLOYS

Using the trained NN-ML model, we calculated the energy versus volume (*E-V*) curves of some Fe-Si crystal structures, and we validated the accuracy of the NN-ML to reproduce the energies of DFT. From the comparison of the calculation results shown in Fig. 3, it can be found that the trained NN-ML model predicts excellently the *E-V* curves of relevant Fe-Si crystal structures. The equilibrium lattice constants of the crystalline phases obtained from the NN-ML potential are also

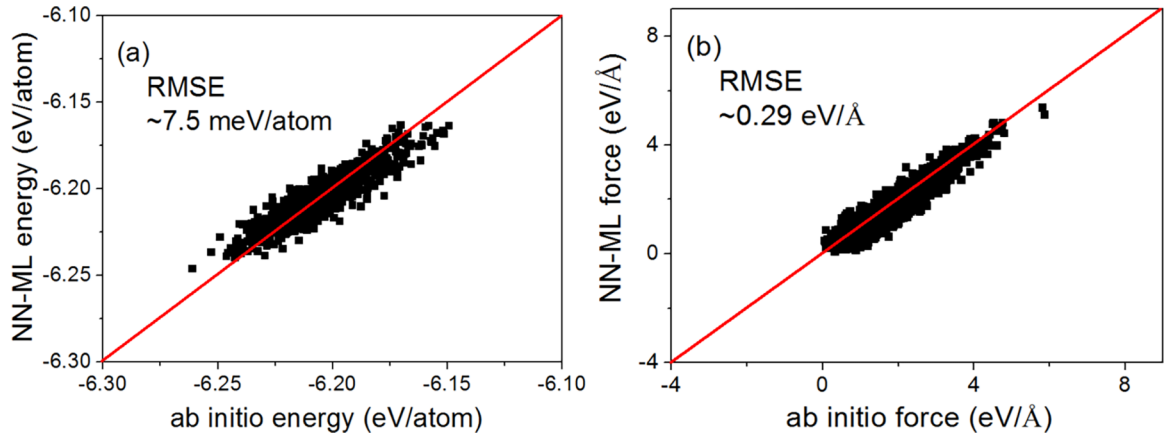

FIG. 2. The comparison of the energies and the magnitude of the forces predicted by the trained NN-ML model and *ab initio* calculation results for the $Fe_{30}Si_{70}$ alloy at a temperature of 1300 K.

in good agreement with the DFT results and experimental data, as shown in Table III. These good agreements suggest that the NN-ML potential is transferable with respect to various bonding environments in Fe-Si crystal phases.

We also calculate the energy convex hull for Fe-Si binaries using the NN-ML potential, and we compare the results with those from DFT calculations. The formation energies of the Fe-Si binary compounds are defined as

$$E_{\text{form}}(\text{Fe}_x\text{Si}_y) = [E(\text{Fe}_x\text{Si}_y) - xE(\text{Fe}) - yE(\text{Si})]/(x+y),$$

where $E(\text{Fe}_x\text{Si}_y)$ is the total energy of the Fe_xSi_y compound, and E(Fe) and E(Si) are the per atom energy of the ground state of Fe and Si crystal, respectively. The bcc Fe ($Im\bar{3}m$) structure and diamond Si ($Fd\bar{3}m$) structure were used as

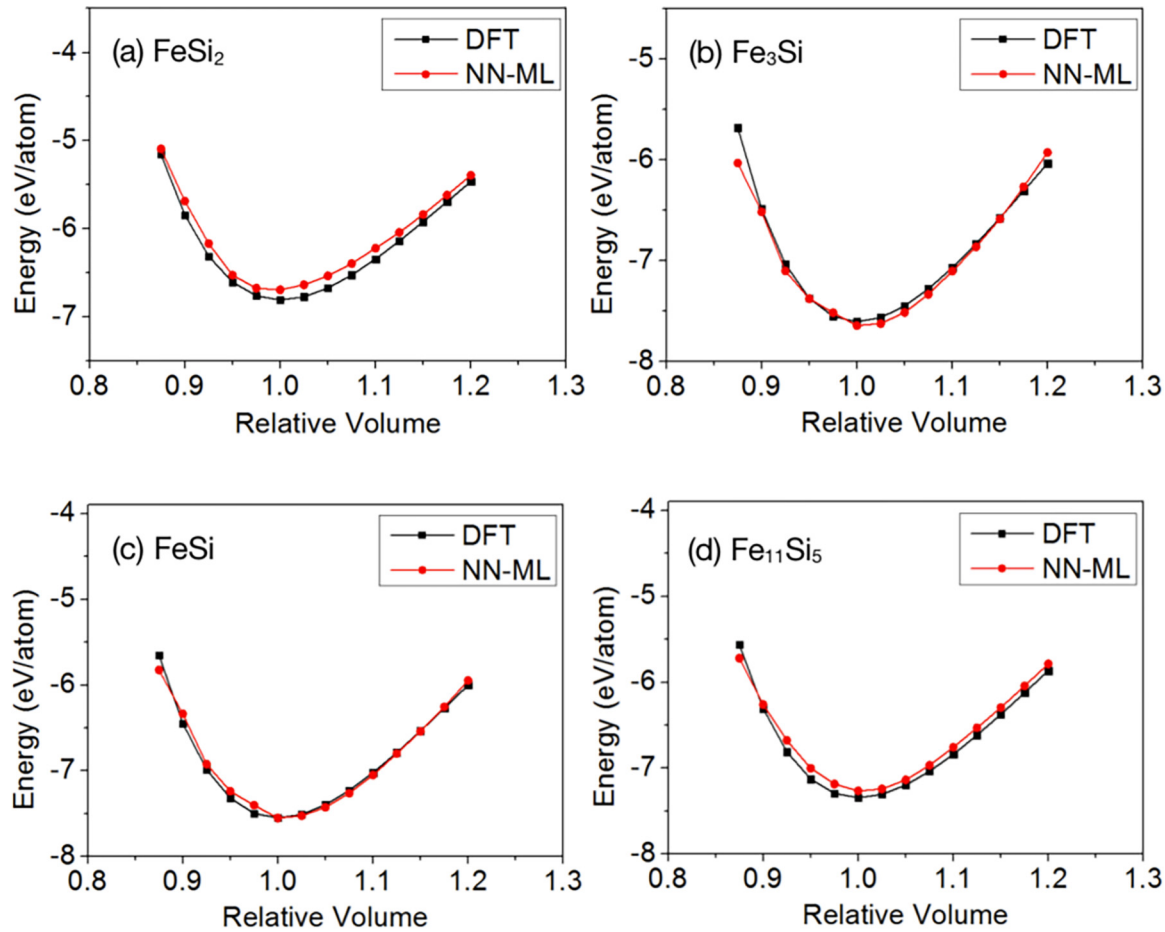

FIG. 3. Curves of energy vs volume obtained from DFT and NN-ML potential calculations for some crystal structures of the Fe-Si system. The volume is in units of the equilibrium volume V_0.

TABLE III. A list of lattice constants (in units of Å) obtained from the experimental measurement, the DFT calculations, and the calculations using the NN-ML potential for the four Fe-Si crystals.

Compound	Experiment	DFT	NN-ML
Fe_3Si	$a = b = c = 5.66$ [50]	$a = b = c = 5.52$	$a = b = c = 5.53$
Fe_5Si_3	$a = b = 6.75$, $c = 4.74$ [51]	$a = b = 6.55$, $c = 4.71$	$a = b = 6.63$, $c = 4.66$
$FeSi_2$	$a = 9.86$, $b = 7.79$, $c = 7.83$ [52]	$a = 9.88$, $b = 7.76$, $c = 7.81$	$a = 9.86$, $b = 7.73$, $c = 7.74$
FeSi	$a = b = c = 4.48$ [53]	$a = b = c = 4.44$	$a = b = c = 4.45$

references in the convex hull construction. The atomic structures are optimized using the conjugate gradient algorithm in the NN-ML potential and DFT calculations. The comparison results are shown in Fig. 4. For the stable crystalline phases (i.e., Fe_3Si, FeSi, and $FeSi_2$) used for the training data, we can see from the figure that the formation energies calculated by the NN-ML potential are in good agreement with the results by DFT. In addition, we also calculated the formation energies of crystalline structures $FeSi_3$, which was not included in the training data set. The result shows that the formation energy of the $FeSi_3$ binary compound calculated by NN-ML is also very close to that of the DFT calculation. These results verify the accuracy and transferability of the NN-ML potential.

The melting temperature of the lowest-formation energy phase, i.e., FeSi, is studied using the developed NN-ML potential to test the predictive capability of the potential since melting temperatures are not explicitly included in the training data set. The melting temperature is determined through the solid/liquid coexistence MD simulation [54]. An initial FeSi(001)/liquid interface sample of 3600 atoms with 1800 atoms in crystalline structures and 1800 atoms in liquid phase is prepared at $T = 1600$ K (about 80 K below the experimental melting point) under zero pressure by an *NPT* ensemble. Then the solid/liquid coexistence MD simulations are carried out using an *NVE* ensemble where the total energy is adjusted by scaling the velocities of the atoms. By varying the total energy, the solid/liquid interface exhibits three different behaviors, i.e., crystallization, solid/liquid coexistence, or melting as shown in Figs. 5(b)–5(d), respectively. The melting temperature is calculated by time averaging of kinetic energy for the last 60 ps of MD simulation in the solid/liquid coexistence sample shown in Fig. 5(c). The melting temperature determined in this way is about 1812 K, which is 129 K (7.7%) higher than the experimental value (1683 K [55]). Since the NN-ML potential is trained using the DFT calculation data, the slight overestimation of the melting temperature would partially be attributed to an overestimation of binding energy by DFT calculation.

To further verify the transferability and reliability of the NN-ML potential, we apply the potential in MD simulations using the LAMMPS package [56] to study the structures of $Fe_{11}Si_5$, FeSi, and $Fe_{10}Si_{90}$ liquids, which cover from Fe-rich to Fe poor compositions, and we compare the results with those from AIMD simulations. The NN-ML potential MD

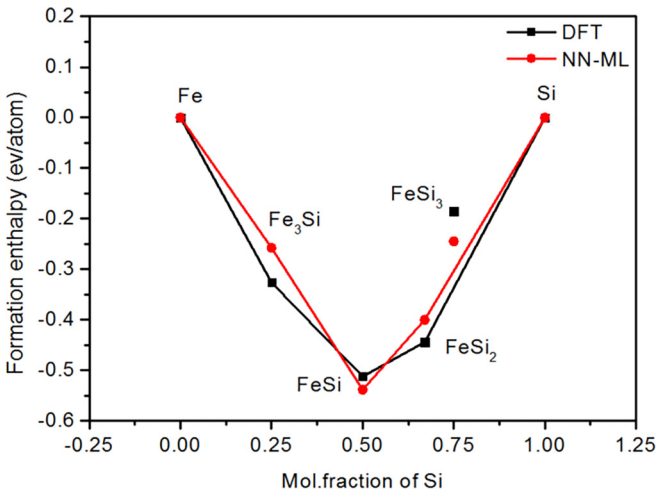

FIG. 4. Formation energy of the Fe-Si crystalline phases calculated by the DFT and NN-ML potential.

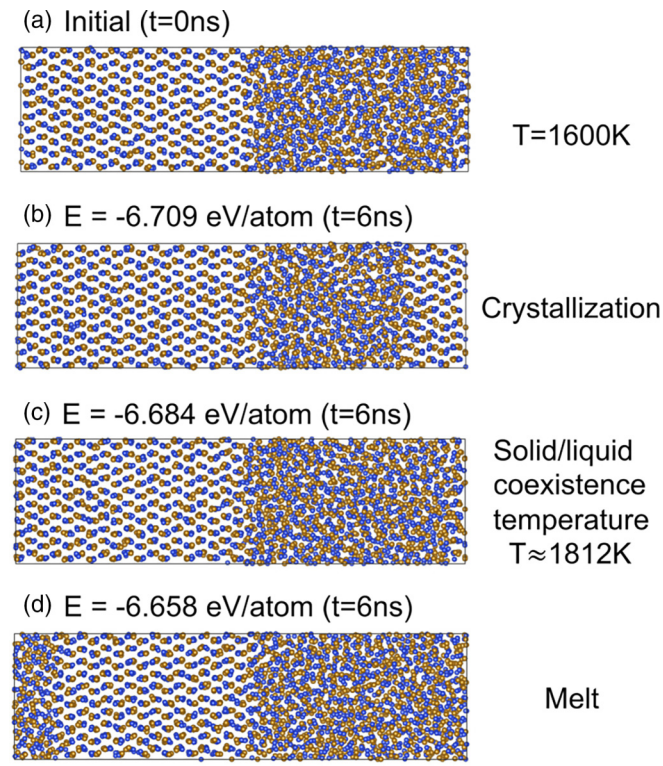

FIG. 5. (a) Initial FeSi(001)/liquid configuration, where the golden and blue balls are Fe and Si atoms, respectively. (b)–(d) The configurations (after 6 ns simulation time) for the FeSi(001)/liquid sample at different total energies. The sample in (b) begins to grow crystal at the interface, while the sample in (d) starts to melt at the interface. The sample in (c) is in a solid/liquid equilibrium state where the temperature of the melting point is about 1812 K.

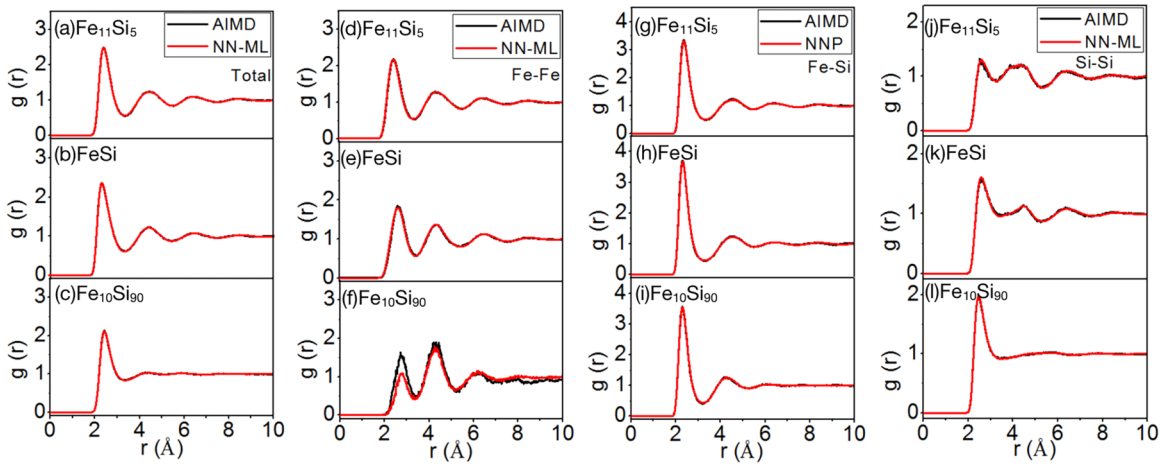

FIG. 6. Comparison of the pair distribution functions of (a)–(c) total, (d)–(f) Fe-Fe pairs, (g)–(i) Fe-Si pairs, and (j)–(l) Si-Si pairs of three Fe-Si alloy liquids at 2000 K.

and AIMD simulations are performed at the same conditions, i.e., using an *NVT* ensemble with 200 atoms in a cubic box of the same volume at each composition and with periodic boundary conditions, and at T= 2000 K, which is controlled by a Nosé-Hoover thermostat. As shown in Fig. 6, the total pair distribution functions (PDFs) and Fe-Fe, Fe-Si, and Si-Si partial PDFs of the three liquids obtained from NN-ML MD simulations agree well with those from AIMD simulations at the same conditions, except some discrepancy for the Fe-Fe partial PDF in $Fe_{10}Si_{90}$ liquid. This discrepancy would be due to the small number of Fe atoms in the simulation cell, which cause poor statistics for Fe-Fe partial PDF. The overall good agreement between the NN-ML MD and AIMD results indicates that the NN-ML potential is accurate for MD simulation of high-temperature liquid Fe-Si alloys over a wide range of compositions.

To see how reliable are the predictions from the developed NN-ML interatomic potential, the temperature dependence of viscosity in liquids $Fe_{70}Si_{30}$ and $Fe_{62}Si_{38}$ is investigated using MD simulations with the NN-ML potential, and the simulation results are compared with the experimental data from Ref. [57]. The MD simulations are performed in an isothermal-isobaric (*NPT*) ensemble with the number of atoms N= 5000 and at zero pressure. A Nosé-Hoover thermostat is used to control the pressure and temperature. Periodic boundary conditions in all three directions are applied, and the MD time step is 2.5 fs. High-temperature liquids are first prepared by the MD simulations at 2000 K for 120 ps. Then the liquids are cooled down to lower temperatures step-by-step to study the temperature dependence of viscosity. At each temperature, 25 ps MD simulations are performed to equilibrate the liquid at the temperature, followed by another 25 ps of simulation to calculate viscosity. The viscosity is calculated from the equilibrium MD simulation calculation based on the Green-Kubo formula [58],

$$\eta = \frac{V}{k_B T}\int_0^\infty \langle p_{\alpha\beta}(0)p_{\alpha\beta}(t)\rangle dt,$$

where V is the volume of the simulation box, $p_{\alpha\beta}$ is the off-diagonal component of the pressure tensor, and $\langle\cdots\rangle$ means the average that is taken over all off-diagonal components ($\alpha\beta$ is xy, xz, or yz) and all time origins.

As shown in Fig. 7, with the decrease of liquid temperature, the viscosity of $Fe_{70}Si_{30}$ and $Fe_{62}Si_{38}$ liquid alloys gradually increases, which is consistent with the experimental results in Ref. [57], although the numerical value is slightly offset. We note that viscosities are not explicitly included in the training. These results indicate that the predictions from the developed NN-ML potential are reliable.

To further verify that the developed NN-ML Fe-Si potential is suitable for undercooled liquid and glass simulations, we compare the NN-ML and *ab initio* MD results for $Fe_{11}Si_5$ at 1000 K (which is close to the glass-transition temperature). It can be seen from Fig. 8 that the RMSE for the energies and the magnitude of forces of the $Fe_{11}Si_5$ alloy at 1000 K are acceptable. The total PDFs and Fe-Fe, Fe-Si, and Si-Si partial PDFs of the alloy (shown in Fig. 9) obtained from the NN-ML MD simulations also agree well with those from AIMD simulations at the same conditions.

IV. STRUCTURES OF Fe-Si ALLOYS UNDER RAPID SOLIDIFICATION BY MD SIMULATIONS

The accuracy and efficiency of the developed NN-ML potential enable us to perform extensive MD simulations with a larger number of atoms and a longer simulation time to gain useful insights into the structures of Fe-Si alloys with various compositions under a rapid solidification process. In the MD simulations, an *NPT* (N= 5000 atoms, P= 0) ensemble and a Nosé-Hoover thermostat are used. The time step for the MD simulations is 3 fs and the periodic boundary conditions are used in the three directions. Above the melting point, the liquid Fe-Si alloys are first annealed at 2000 K for 30 ps to reach equilibrium and then cooled down to 100 K at a cooling rate of 10^{11} K/s.

The evolutions of instantaneous potential energies (E–$3k_BT$) with the temperature [59–61] for the Fe-Si alloys of different compositions at the cooling rate of 10^{11} K/s are shown in Fig. 10. As can be seen from the figure, in the high-temperature section with temperature exceeding 1000 K, the potential energies of $Fe_{11}Si_5$ and FeSi alloys

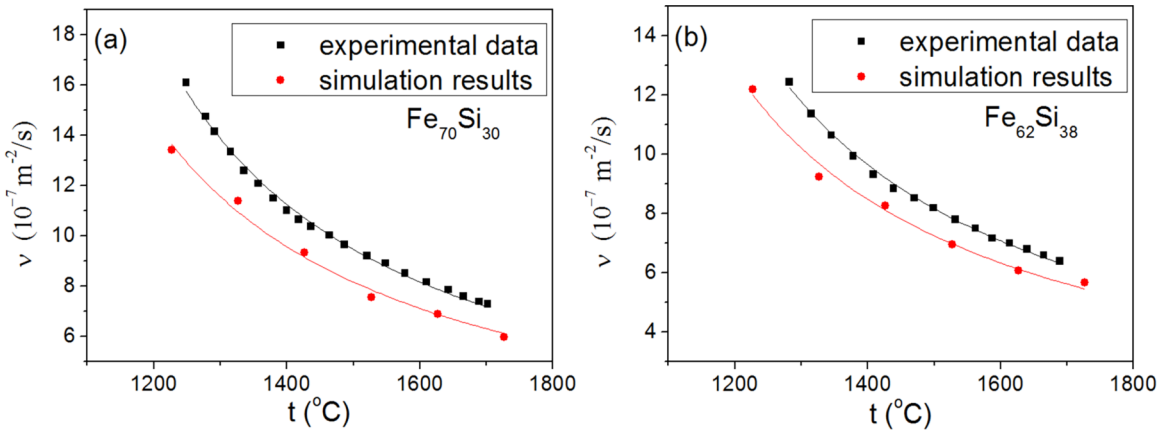

FIG. 7. The comparison of experimental data and simulation results of viscosity of $Fe_{70}Si_{30}$ and $Fe_{62}Si_{38}$ liquid alloys at different temperatures.

decrease significantly with the decrease of temperature. However, when the temperature drops below 1000 K, the potential energies decrease slowly. This evolution of potential energies suggests a glass transition, and the glass transition temperatures of $Fe_{11}Si_5$ and FeSi alloys are similar and around 1000 K. As the Si content continues increasing to 70% and 80%, the potential energies decrease slower with temperature in the high-temperature stage, and the glass transition gradually weakens and shifts to lower temperatures. Finally, as the Si content reaches 90%, there is an abrupt drop in instantaneous potential energy for the $Fe_{10}Si_{90}$ alloy at a temperature around 600 K, indicating that a crystallization process occurs during the rapid cooling.

To gain more insights into the local ordered structures in the rapid solidified Fe-Si alloys obtained from the MD simulations, the short-range-order (SRO) motifs and corresponding fractions in the samples at 300 K are quantified by using the cluster alignment method developed previously [62,63]. For each Fe or Si atom in the samples, a cluster of atoms in a sphere within a radius R around this atom is extracted from the MD sample. This cluster is then aligned with a given template cluster to quantify the similarity of the cluster to the template cluster. The radius R is adjusted so that each cluster contains a few more atoms than the number of atoms in the template cluster. The alignment is proceeded by overlapping the center atom of the cluster with the center atom of the template, and then rotating the cluster around the center atom to minimize the relative distances of the corresponding atoms in the cluster and template. The alignment score is determined by the overall minimum of these relative distances. Therefore, the smaller the alignment score is, the more similarity there is between the cluster and the template. A cutoff score (usually taken as 0.16) is then applied to determine if the cluster can be classified as the template motif. The choice of cutoff score of 0.16 is mainly guided by considering the structure distortion due to the thermal fluctuation effect. This value is estimated by the half-width of the first peak in the Fe-Si pair distribution function divided by the average Fe-Si bond length in the sample at room temperature. For more details of the cluster alignment method, we refer the readers to our previous publications [62,63].

The alignment score distributions with respect to some given templates as indicated for the $Fe_{11}Si_5$, $Fe_{30}Si_{70}$, and $Fe_{10}Si_{90}$ MD samples at room temperature are shown in Fig. 11. The selection of templates is crucial for the alignment analysis. First, the six commonly observed SRO motifs

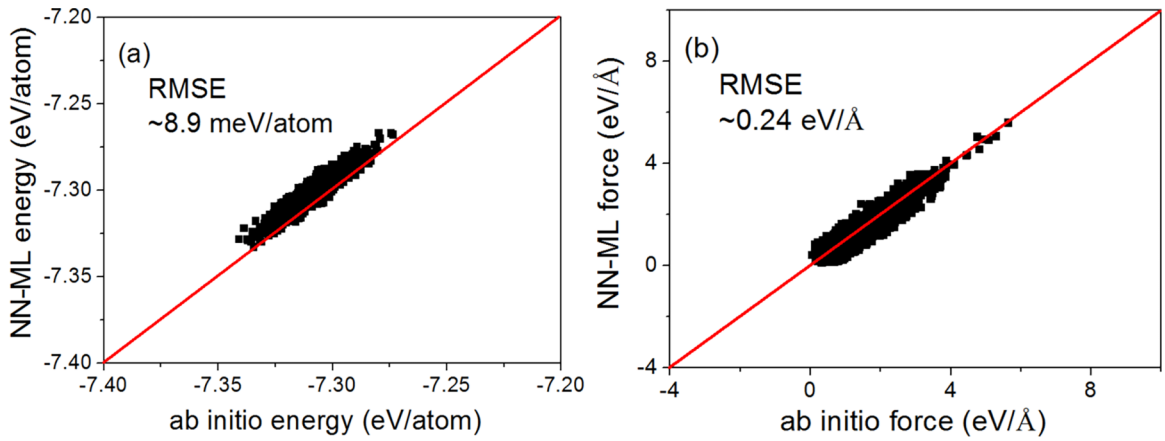

FIG. 8. The comparison of the energies and the magnitude of the forces predicted by the trained NN-ML model and *ab initio* calculation results for the $Fe_{11}Si_5$ alloy at the glass-transition temperature of 1000 K.

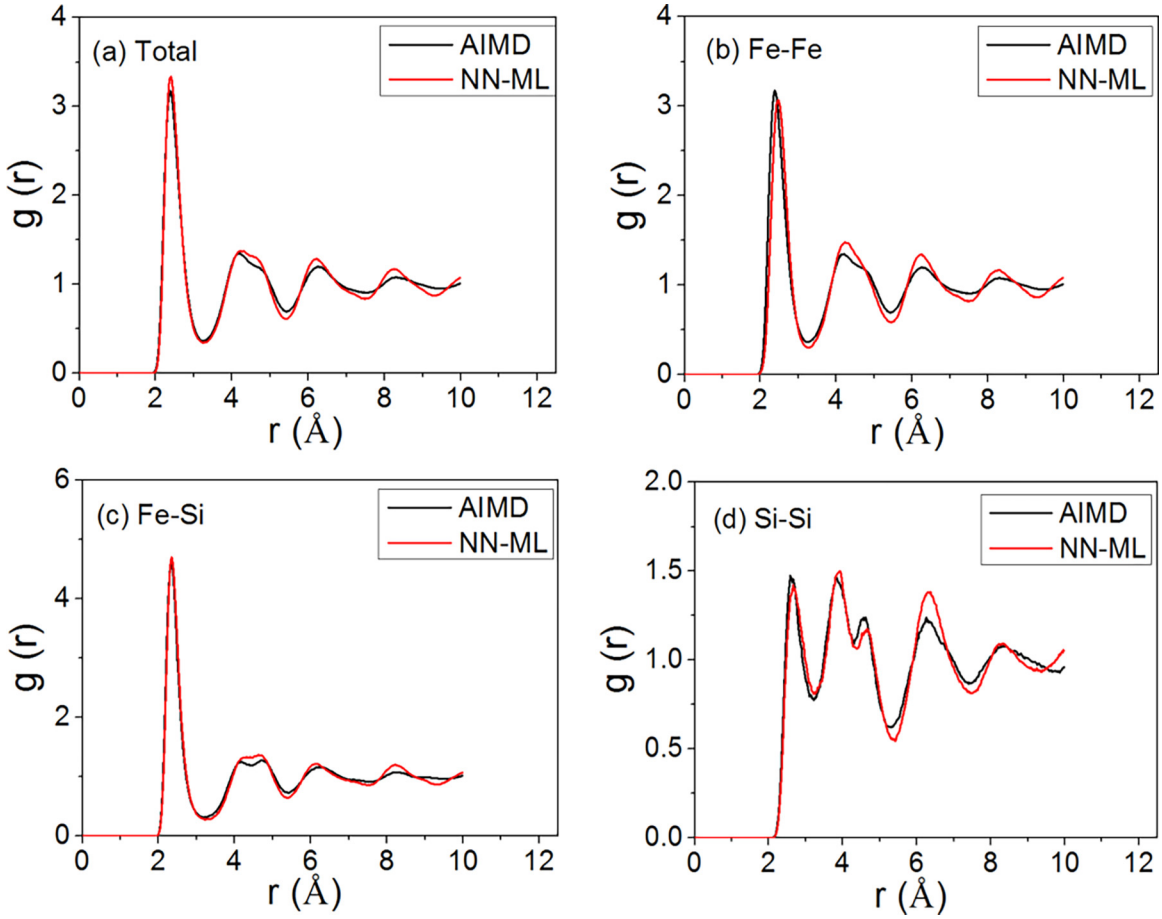

FIG. 9. The comparison of the pair distribution functions from simulations by NN-ML MD and AIMD for the $Fe_{11}Si_5$ alloy at the glass-transition temperature of 1000 K.

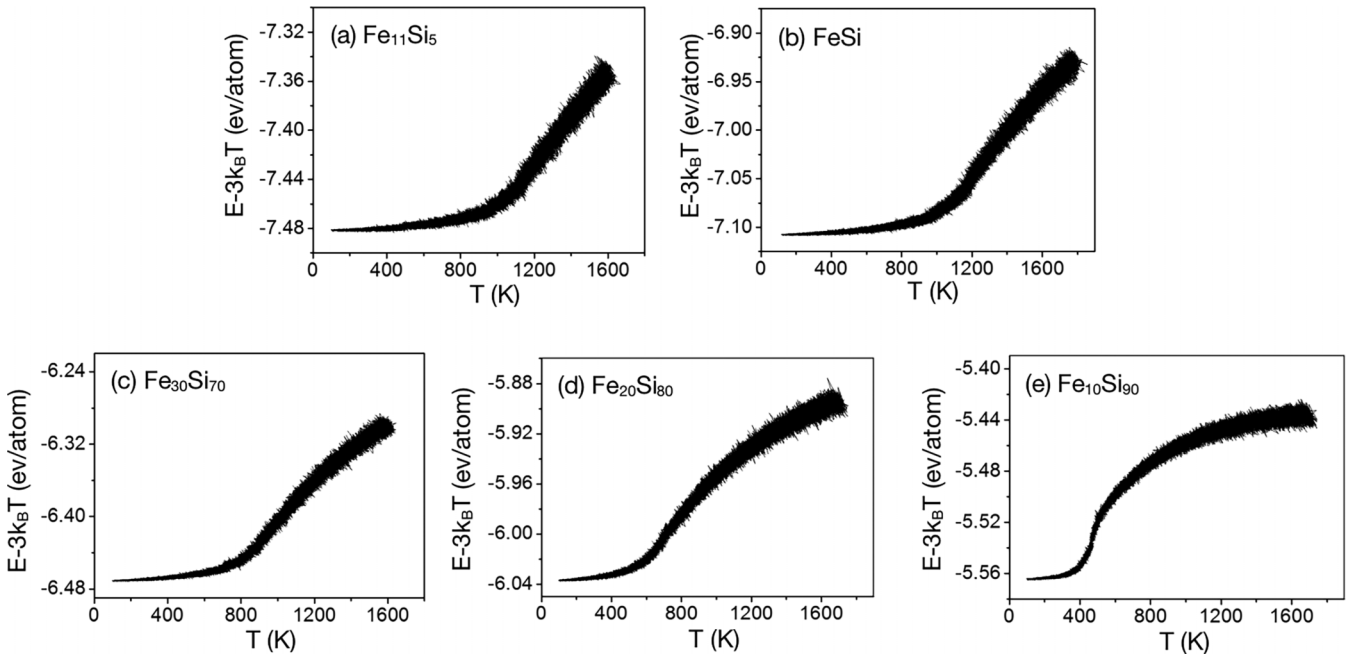

FIG. 10. The instantaneous potential energies as a function of temperature for Fe-Si alloys at the cooling rate of 10^{11} K/s.

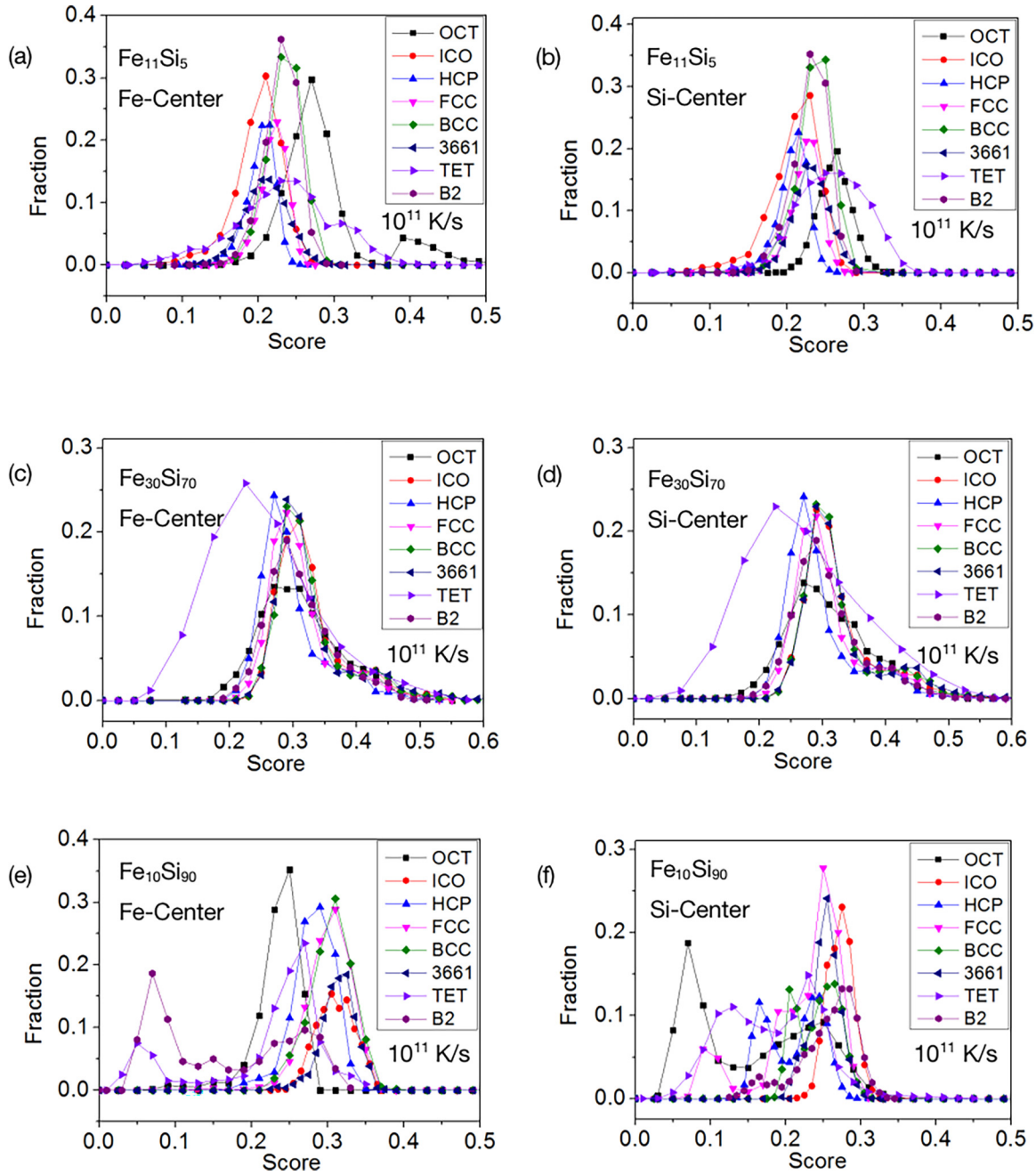

FIG. 11. The distribution of alignment scores against various selected motifs for $Fe_{11}Si_5$, $Fe_{30}Si_{70}$ and $Fe_{10}Si_{90}$ alloys.

[i.e., icosahedra (ICO), octahedral (OCT), tetrahedral (TET), face-centered-cubic (FCC), body-centered-cubic (BCC), and hexagonal close-packed (HCP)] are used as templates for the alignment analysis. In addition, the "B2" motif, i.e., the partially ordered α_2 phase in the Fe-Si phase diagram [64], and the "3661" motif usually seen in the metallic glasses (which has the structure of a top triangle, two consecutive hexagons in the middle, and a single atom at the bottom [65]), are also included in the templates list. For the Fe-centered and Si-centered clusters in $Fe_{11}Si_5$, we can see that the alignment scores are between 0.2 and 0.3, indicating that the degree of SRO is very weak in this structure. As for the $Fe_{30}Si_{70}$ alloys, most alignment scores of Fe-centered and Si-centered clusters are around 0.3, except for the alignment scores against the TET template. Although the distribution of the alignment scores with respect to the TET template is very wide and peaks around 0.2, there are substantial fractions of scores below the cutoff score of 0.16 for both Fe- and Si-centered clusters. These results suggest that TET is the dominant SRO motif in the $Fe_{30}Si_{70}$ alloy upon rapid solidification from a liquid state. By summing over the clusters that have an alignment score on the TET template less than the cutoff score of 0.16, we found that about 11% of Fe-centered clusters and about 9.8% of Si-centered clusters in the $Fe_{30}Si_{70}$ samples can be classified as TET motif. The spatial distributions of these TET clusters in the sample are shown in Fig. 12. It can be seen that Fe-centered and Si-centered clusters are evenly distributed in the sample. As the proportion of Fe atoms in the alloy is

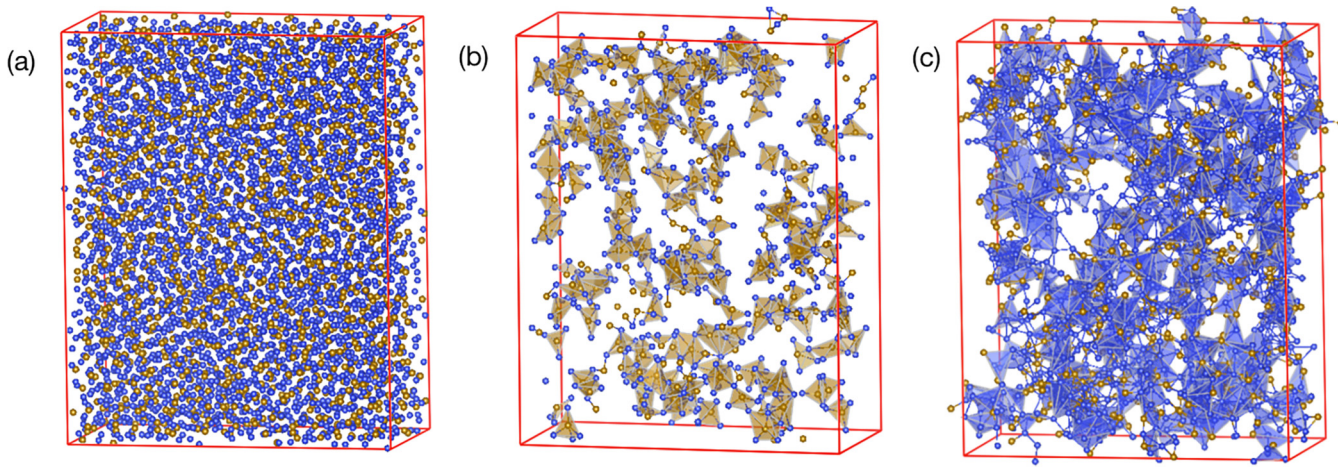

FIG. 12. (a) The $Fe_{30}Si_{70}$ alloy at 300 K, in which the golden balls denote the Fe atoms and the blue ones represent the Si atoms. The spatial distributions of TET templates in (b) Fe-centered and (c) Si-centered clusters of the sample.

relatively small, only 30%, it seems that Fe-centered clusters are relatively sparse. It is interesting to note that as the Si content becomes richer, strong SROs emerge in the rapidly solidified $Fe_{10}Si_{90}$ alloy. The distribution of alignment scores with respect to the B2 template for the Fe-centered clusters exhibits a strong and sharp peak around 0.07, suggesting a strong B2-type order around the Fe atoms in the sample. Meanwhile, alignment of the Fe-centered cluster against the TET template also shows a sharp peak around 0.05, indicating that TET is also a strong SRO motif for the Fe-centered cluster in the rapidly quenched $Fe_{10}Si_{90}$ sample. Strong structural order can also be observed for Si-centered clusters in the sample. While the OCT is obviously the dominant SRO motif around the Si atoms with a strong and sharp peak in its alignment score around 0.07, the TET SRO motif is also very strong, as can be seen from the alignment score distribution shown in Fig. 11(f).

We further analyzed the development of the dominant Fe-centered B2 and TET clusters as well as Si-centered OCT and TET clusters in the $Fe_{10}Si_{90}$ sample as the temperature is lowered from 500 to 300 K during the rapid solidification process. Figure 13 shows the population of these dominated clusters as a function of temperature, where the cutoff score of 0.16 is used to assign the clusters to the corresponding templates. If a cluster has a score lower than 0.16 for more than one template, the template that gives the lowest alignment score is assigned to the cluster. As can be seen from Fig. 13(a), the most dominant Fe-centered B2 motif developed rapidly as the temperature was lowered. When the liquid $Fe_{10}Si_{90}$ alloy is cooled to 500 K, the amount of the B2 clusters is still relatively small, accounting for only about 8.8% of all the Fe-centered clusters. As the alloy continues cooling, the fraction of the B2 clusters increases sharply and reaches about 40% at 400 K and a high value of 53.7% at 300 K. Similarly, as the most dominant motif of Si-centered clusters, the fraction of OCT is only a few percent when cooling to 500 K, even far below that of TET, which is about 20% at 500 K. However, with the temperature is reduced to 400 and 300 K, the percentage of OCT clusters grows dramatically, reaching 42% at 400 K and 50.7% at 300 K, as one can see from Fig. 13(b). In comparison, the development of TET SRO for both Fe-centered and Si-centered clusters as a function of temperature is more gradually and reaches about 20% and 40%, respectively, at T= 300 K. The percentage of Si-centered TET clusters is about twice that of Fe-centered TET clusters at each temperature.

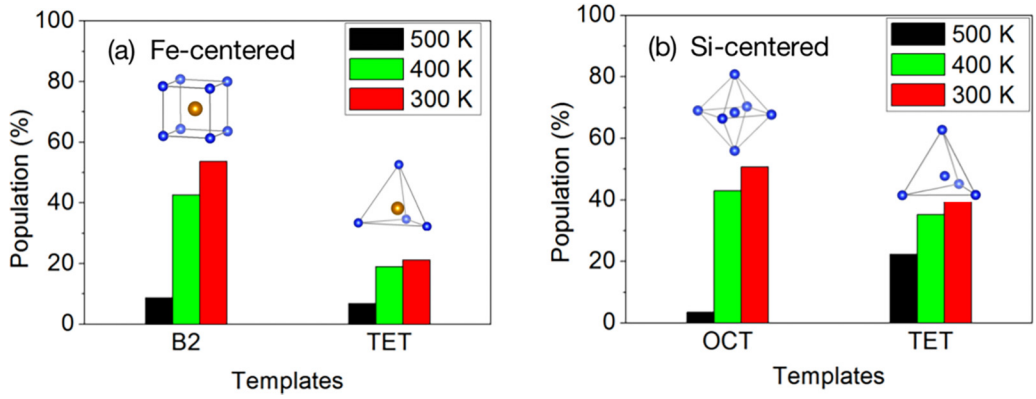

FIG. 13. (a) Populations of Fe-centered B2 and Fe-centered TET clusters in the sample of $Fe_{10}Si_{90}$; (b) populations of Si-centered OCT and Si-centered TET clusters in the sample of $Fe_{10}Si_{90}$.

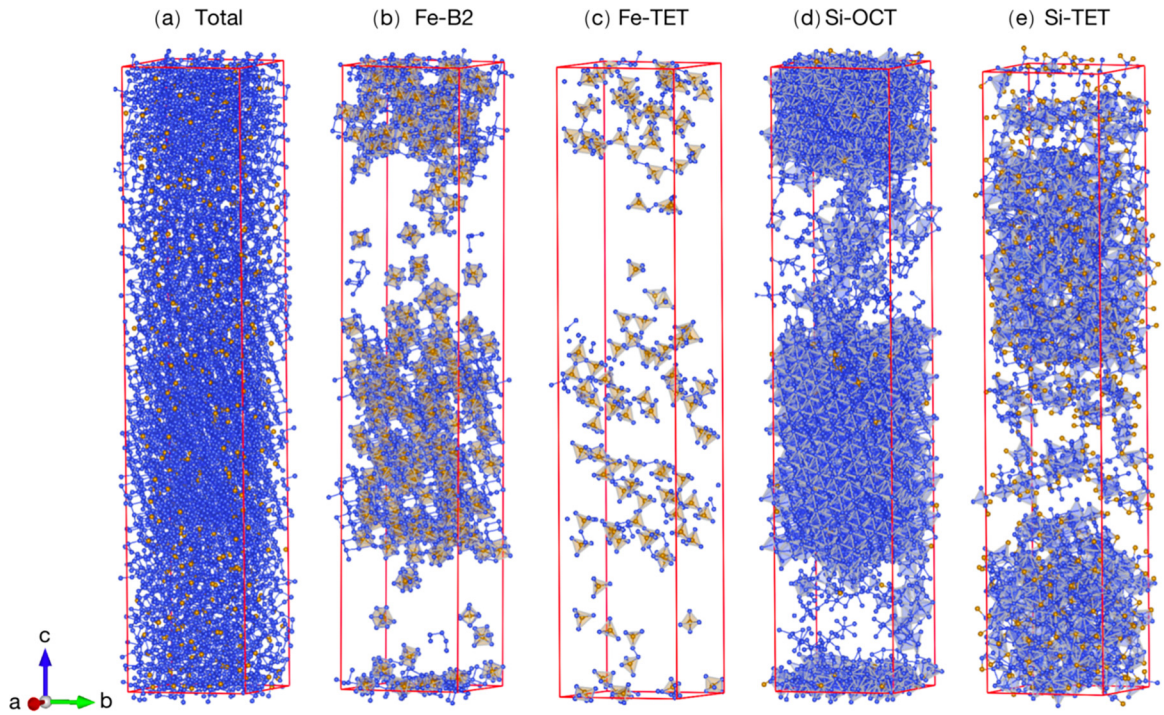

FIG. 14. (a) The $Fe_{10}Si_{90}$ alloy at 300 K, in which the golden balls denote the Fe atoms and the blue ones represent the Si atoms. Parts (b) and (c) exhibit the distribution of B2 and TET templates in Fe-centered clusters of the $Fe_{10}Si_{90}$ alloy at 300 K. Parts (d) and (e) exhibit the distribution of OCT and TET templates in Si-centered clusters of the $Fe_{10}Si_{90}$ alloy at 300 K.

The spatial distributions of the dominant Fe-centered B2 and TET clusters and the Si-centered OCT and TET clusters in the $Fe_{10}Si_{90}$ at T= 300 K are shown in Fig. 14. As one can see from Fig. 14(a), where all these clusters in the sample are plotted, some sections in the $Fe_{10}Si_{90}$ sample (i.e., the sections in the middle, top, and bottom of the sample) exhibit a well-crystallized order. Interestingly, all of the Fe-centered B2 and TET clusters are almost located in the crystallization sections, as shown in Figs. 14(b) and 14(c). For the Si-centered clusters, the crystalline section is mainly occupied by the OCT clusters, while the amorphous section is mainly occupied by TET clusters. When we roughly divide the Si and Fe atoms in the sample into a crystalline group and a glass group according to their coordinates along the c axis, as shown in Fig. 14, we find that the ratio of Fe and Si in the crystallization section is about 1:9.2, while the ratio of Fe and Si in the amorphous region is about 1:8.3. This analysis result suggests that crystallization of Fe-Si alloys under rapid solidification with a cooling rate of 10^{11} K/s would require more than 90% of Si concentration. This result is also consistent with our simulation results discussed above, i.e., that the sample with 70% and 80% of Si tends to end up with amorphous structures under the rapid cooling condition, but the glass-forming tendency tends to weaken when the Si concentration is increased.

V. SUMMARY

In summary, a NN-ML interatomic potential for Fe-Si alloys is developed by using the deep neural network learning method. The energies and forces of Fe-Si alloys as well as elemental Fe and Si structures, in both randomly distorted crystalline states and liquid state at various temperature, have been calculated by the first-principles DFT method to generate sufficient data for the ML training. The developed NN-ML potential has been demonstrated to describe accurately the structures and energies of the Fe-Si alloys in both crystalline structures and liquid states, in comparison with the results from first-principles DFT calculations and AIMD simulations. The melting temperature of the FeSi phase and the viscosity of $Fe_{70}Si_{30}$ and $Fe_{62}Si_{38}$ liquid alloys at different temperatures predicted by the developed NN-ML interatomic potential are also in good agreement with experimental data. The accuracy and efficiency of the NN-ML potential enable us to perform reliable MD simulations with a large number of atoms and a long simulation time to systemically investigate the structures of Fe-Si alloys with various composition concentrations under the rapid solidification conditions. Glass formation or crystallization under rapid cooling are found to be strongly dependent on the concentration ratio of Fe and Si in the sample. Fe-rich samples are found to have strong glass-forming ability, while Si-rich samples exhibit more of a tendency towards crystallization. SRO in the rapid solidification samples is analyzed and described quantitatively using the cluster alignment method. The results show that there are no dominated clusters in the $Fe_{11}Si_5$ alloy, indicating that this alloy has a high degree of structural disorder. The degrees of structural SRO are enhanced as the Si concentration increases. A significant amount TET SRO is observed for both Fe-centered and Si-centered clusters in the $Fe_{30}Si_{70}$ sample. When the Si concentration reaches 90%, while the TET SRO around both Fe and Si atoms (especially around Si atoms) continues to grow in the $Fe_{10}Si_{90}$ sample, Fe-centered B2 clusters and Si-centered OCT clusters

develop even more rapidly as the temperature is lowered, and eventually lead to the partial crystallization of the $Fe_{10}Si_{90}$ sample at 300 K.

ACKNOWLEDGMENTS

Work at Ames Laboratory was supported by the U.S. Department of Energy (DOE), Office of Science, Basic Energy Sciences, Materials Science and Engineering Division including a grant of computer time at the National Energy Research Scientific Computing Centre (NERSC) in Berkeley, CA. Ames Laboratory is operated for the U.S. DOE by Iowa State University under Contract No. DE-AC02-07CH11358. C. Zhang acknowledges financial support from the National Natural Science Foundation of China (Grant No. 11874318) and GHfund B (202302029995).

[1] S. Paschen, E. Felder, M. A. Chernikov, L. Degiorgi, H. Schwer, and H. R. Ott, Low-temperature transport, thermodynamic, and optical properties of FeSi, Phys. Rev. B **56**, 12916 (1997).

[2] J. Kudrnovsky, N. E. Christensen, and O. K. Andersen, Electronic structures and magnetic moments of $Fe_{3+y}Si_{1-y}$ and $Fe_{3-x}V_xSi$ alloys with DO_3-derived structure, Phys. Rev. B **43**, 5924 (1991).

[3] B. H. Zhang, Z. Wang, Y. N. Zhang, and R. Q. Wu, Effect of structural disordering on magnetic and magneto-optical properties of Fe_3Si, Phys. Rev. Mater. **3**, 095602 (2019).

[4] T. Jarlborg, Low-temperature properties of ε-FeSi from ab initio band theory, Phys. Rev. B **51**, 11106 (1995).

[5] I. Nishida, Study of semiconductor-to-metal transition in Mn-doped $FeSi_2$, Phys. Rev. B **7**, 2710 (1973).

[6] D. Leong, M. Harry, K. J. Reeson, and K. P. Homewood, A silicon/iron-disilicide lightemitting diode operating at a wavelength of 1.5 μm, Nature (London) **387**, 686 (1997).

[7] K. Nomura, H. Reuther, E. Richter, and Y. Ujihira, Magnetic structure of Fe−Si−Al films implanted with Al and N ions, J. Radioanal. Nucl. Chem. **190**, 299 (1995).

[8] T. Komatsu, Y. Sakemi, K. Shimagami, K. Matusita, and M. Miyazaki, Mössbauer study of Fe magnetic state at the interface between Fe-Al-Si thin films and crystallized glass substrate, J. Mater. Sci. **7**, 101 (1996).

[9] Y. Yoshizawa, S. Oguma, and K. Yamauchi, New Fe-based soft magnetic alloys composed of ultrafine grain structure, J. Appl. Phys. **64**, 6044 (1988).

[10] Y. Yoshizawa, K. Yamauchi, T. Yamane, and H. Sugihara, Common mode choke cores using the new Fe-based alloys composed of ultrafine grain structure, J. Appl. Phys. **64**, 6047 (1988).

[11] Y. Yoshizawa and K. Yamauchi, Fe-based soft magnetic alloys composed of ultrafine grain structure, Mater. Trans. JIM **31**, 307 (1990).

[12] J. Karel, D. S. Bouma, J. Martinez, Y. N. Zhang, J. A. Gifford, J. Zhang, G. J. Zhao, D. R. Kim, B. C. Li, Z. Y. Huang, R. Q. Wu, T. Y. Chen, and F. Hellman, Enhanced spin polarization of amorphous Fe_xSi_{1-x} thin films revealed by Andreev reflection spectroscopy, Phys. Rev. Mater. **2**, 064411 (2018).

[13] M. Milosavljevic, G. Shao, N. Bibic, C. N. McKinty, C. Jeynes, and K. P. Homewood, Amorphous-iron disilicide: A promising semiconductor, Appl. Phys. Lett. **79**, 1438 (2001).

[14] M. Milosavljevic, G. Shao, N. Bibic, C. N. McKinty, C. Jeynes, and K. P. Homewood, Synthesis of amorphous $FeSi_2$ by ion beam mixing, Nucl. Instrum. Methods Phys. Res. B **188**, 166 (2002).

[15] M. Milosavljevic, G. Shao, R. M. Gwilliam, Y. Gao, M. A. Lourenco, R. Valizadeh, J. S. Colligon, and K. P. Homewood, Semiconducting amorphous $FeSi_2$ layers synthesized by co-sputter deposition, Thin Solid Films **461**, 72 (2004).

[16] L. Antwis, L. Wong, A. Smith, K. Homewood, C. Jeynes, and R. Gwilliam, Optimization and characterization of amorphous iron disilicide formed by ion beam mixing of Fe/Si multilayer structures for photovoltaic applications, AIP Conf Proc. **1321** 278 (2011).

[17] M. B. Stearns, Internal magnetic fields, isomer shifts, and relative abundances of the various Fe sites in FeSi alloys, Phys. Rev. **129**, 1136 (1963).

[18] M. B. Stearns, Measurement of conduction-electron spindensity oscillations in ordered FeSi alloys, Phys. Rev. B **4**, 4069 (1971).

[19] E. P. Elsukov, G. N. Konygin, V. A. Barinov, and E. V. Voronina, Local atomic environment parameters and magnetic properties of disordered crystalline and amorphous iron-silicon alloys, J. Phys.: Condens. Matter **4**, 7597 (1992).

[20] N. I. Kulikov, D. Fristot, J. Hugel, and A. V. Postnikov, Interrelation between structural ordering and magnetic properties in bcc Fe-Si alloys, Phys. Rev. B **66**, 014206 (2002).

[21] Y. Choi, Y. Koo, S. Kwon, and L. Vitos, Ordered phases in Fe-Si alloys: A first-principles study, J. Korean Phys. Soc. **72**, 737 (2018).

[22] M. Rinaldi, M. Mrovec, M. Fähnle, and R. Drautz, Determination of spin-wave stiffness in the Fe-Si system using first-principles calculations, Phys. Rev. B **104**, 064413 (2021).

[23] M. A. Zagrebin, M. V. Matyunina, A. B. Koshkin, V. D. Buchelnikov, and V. V. Sokolovskiy, Ab initio studies of phase transformations in $Fe_{100-x}Si_x$, Phys. Solid State **62**, 739 (2020).

[24] L. Tang, Z. J. Yang, T. Q. Wen, K. M. Ho, M. J. Kramer, and C. Z. Wang, Development of interaomic potential for Al–Tb alloys using a deep neural network learning method, Phys. Chem. Chem. Phys. **22**, 18467 (2020).

[25] L. Verlet, Computer "experiments" on classical fluids. I. thermodynamical properties of Lennard-Jones molecules, Phys. Rev. **159**, 98 (1967).

[26] M. W. Finnis and J. E. Sinclair, A simple empirical N-body potential for transition metals, Philos. Mag. A **50**, 45 (2006).

[27] M. S. Daw and M. I. Baskes, Embedded-atom method: Derivation and application to impurities, surfaces, and other defects in metals, Phys. Rev. B **29**, 6443 (1984).

[28] R. L. C. Vink, G. T. Barkem, W. F. van der Weg, and N. Mousseau, Fitting the Stillinger-Weber potential to amorphous silicon, J. Non-Cryst. Solids **282**, 248 (2001).

[29] M. Z. Hossain, T. Hao, and B. Silverman, Stillinger-Weber potential for elastic and fracture properties in graphene and carbon nanotubes, J. Phys. Condens. Matter **30**, 055901 (2018).

[30] J. Tersoff, New empirical approach for the structure and energy of covalent systems, Phys. Rev. B **37**, 6991 (1988).

[31] H. W. Sheng, E. Ma, and M. J. Kramer, Relating dynamic properties to atomic structure in metallic glasses, JOM **64**, 856 (2012).

[32] Y. Q. Cheng and E. Ma, Atomic-level structure and structure-property relationship in metallic glasses, Prog. Mater. Sci. **56**, 379 (2011).

[33] B. Y. Zhang, Y. Wang, J. C. Chen, J. H. Li, and W. S. Lai, Development of an angular-dependent potential for radiation damage study in Fe-Si solutions, J. Nucl. Mater. **545**, 152643 (2021).

[34] D. J. Hepburn and G. J. Ackland, Metallic-covalent interatomic potential for carbon in iron, Phys. Rev. B **78**, 165115 (2008).

[35] T. Q. Wen, C. Z. Wang, M. J. Kramer, Y. Sun, B. L. Ye, H. D. Wang, X. Y. Liu, C. Zhang, F. Zhang, K. H. Ho, and N. Wang, Development of a deep machine learning interatomic potential for metalloid-containing Pd-Si compounds, Phys. Rev. B **100**, 174101 (2019).

[36] L. Tang, K. M. Ho, and C. Z. Wang, Molecular dynamics simulation of metallic Al–Ce liquids using a neural network machine learning interatomic potential, J. Chem. Phys. **155**, 194503 (2021).

[37] L. Zhang, J. Han, H. Wang, R. Car, and E. Weinan, Deep Potential Molecular Mynamics: A Scalable Model with the Accuracy of Quantum Mechanics, Phys. Rev. Lett. **120**, 143001 (2018).

[38] H. Wang, L. Zhang, J. Han, and E. Weinan, DeePMD-kit: A deep learning package for many-body potential energy representation and molecular dynamics, Comput. Phys. Commun. **228**, 178 (2018).

[39] L. Zhang, D. Y. Lin, H. Wang, R. Car, and E. Weinan, Active learning of uniformly accurate interatomic potentials for materials simulation, Phys. Rev. Mater. **3**, 023804 (2019).

[40] J. J. Wang, H. Shen, R. Y. Yang, K. Xie, C. Zhang, L. Y. Chen, K. M. Ho, C. Z. Wang, and S. Y. Wang, A deep learning interatomic potential developed for atomistic simulation of carbon materials, Carbon **186**, 1 (2022).

[41] N. Xu, Y. Shi, Y. He, and Q. Shao, A deep-learning potential for crystalline and amorphous Lie Si alloys, J. Phys. Chem. C **124**, 16278 (2020).

[42] C. Zhang, L. Tang, Y. Sun, K. M. Ho, R. M. Wentzcovitch, and C. Z. Wang, Deep machine learning potential for atomistic simulation of Fe-Si-O systems under Earth's outer core conditions, Phys. Rev. Mater. **6**, 063802 (2022).

[43] G. Kresse and J. Hafner, Ab initio molecular dynamics for liquid metals, Phys. Rev. B **47**, 558 (1993).

[44] G. Kresse and J. Furthmuller, Efficient iterative schemes for ab initio total-energy calculations using a plane-wave basis set, Phys. Rev. B **54**, 11169 (1996).

[45] D. Vanderbilt, Soft self-consistent pseudopotentials in a generalized eigenvalue formalism, Phys. Rev. B **41**, 7892 (1990).

[46] J. P. Perdew, K. Burke, and M. Ernzerhof, Generalized Gradient Approximation Made Simple, Phys. Rev. Lett. **77**, 3865 (1996).

[47] A. Jain, S. P. Ong, G. Hautier, W. Chen, W. D. Richards, S. Dacek, S. Cholia, D. Gunter, D. Skinner, G. Ceder, and K. A. Persson, Commentary: The Materials Project: A materials genome approach to accelerating materials innovation, APL Mater. **1**, 011002 (2013), Materials Project https://materialsproject.org/.

[48] W. G. Hoover, Canonical dynamics: Equilibrium phase-space distributions, Phys. Rev. A **31**, 1695 (1985).

[49] L. Zhang, J. Han, H. Wang, W. A. Saidi, R. Car, and W. E, in *Advances in Neural Information Processing Systems*, edited by S. Bengio, H. Wallach, H. Larochelle, K. Grauman, N. Cesa-Bianchi, and R. Garnett (Curran Associates, Baixas, 2018), Vol. 31, pp. 4441–4451.

[50] M. Schutte, R. Wartchow, and M. Binnewies, Shape controlling synthesis-formation of Fe_3Si by the reaction of iron with silicon tetrachloride and crystal structure refinement, Z. Anorg. Allg. Chem. **629**, 1846 (2003).

[51] D. Errandonea, D. Santamaría-Perez, A. Vegas, J. Nuss, M. Jansen, P. Rodríguez-Hernandez, and A. Muñoz, Structural stability of Fe_5Si_3 and Ni_2Si studied by high-pressure x-ray diffraction and ab initio total-energy calculations, Phys. Rev. B **77**, 094113 (2008).

[52] J. I. Tani, M. Takahashi, and H. Kido, Lattice dynamicsof β-$FeSi_2$ from first-principles calculations, Physica B **405**, 2200 (2010).

[53] I. G. Wood, W. I. F. David, S. Hull, and G. D. Price, A high-pressure study of ε-FeSi, between 0 and 8.5 GPa, by time-of-flight neutron powder diffraction, J. Appl. Cryst. **29**, 215 (1996).

[54] J. R. Morris, C. Z. Wang, K. M. Ho, and C. T. Chan, Melting line of aluminum from simulations of coexisting phases, Phys. Rev. B **49**, 3109 (1994).

[55] ASM Alloy Phase Diagram Database, https://www.asminternational.org/asm-phase-diagram-resources.

[56] S. Plimpton, Fast parallel algorithms for short-range molecular dynamics, J. Comput. Phys. **117**, 1 (1995).

[57] A. L. Bel'tyukov, V. I. Lad'yanov, and A. I. Shishmarin, Viscosity of Fe–Si melts with silicon content up to 45 at %, High Temp. **52**, 185 (2014).

[58] J. P. Hansen and I. R. McDonald, *Theory of Simple Liquids*, 2nd ed. (Academic, New York, 1986).

[59] Z. J. Yang, L. Tang, T. Q. Wen, K. M. Ho, and C. Z. Wang, Effects of Si solute on the glass formation and atomic structure of Pd liquid, J. Phys.: Condens. Matter **31**, 135701 (2019).

[60] L. Tang, T. Q. Wen, N. Wang, Y. Sun, F. Zhang, Z. J. Yang, K. M. Ho, and C. Z. Wang, Structural and chemical orders in $Ni_{64.5}Zr_{35.5}$ metallic glass by molecular dynamics simulation, Phys. Rev. Mater. **2**, 033601 (2018).

[61] M. I. Mendelev, F. Zhang, Z. Ye, Y. Sun, M. C. Nguyen, S. R. Wilson, C. Z. Wang, and K. M. Ho, Development of interatomic potentials appropriate for simulation of devitrification of $Al_{90}Sm_{10}$ alloy, Model. Simul. Mater. Sci. Eng. **23**, 045013 (2015).

[62] X. W. Fang, C. Z. Wang, Y. X. Yao, Z. J. Ding, and K. M. Ho, Atomistic cluster alignment method for local order mining in liquids and glasses, Phys. Rev. B **82**, 184204 (2010).

[63] Y. Sun, F. Zhang, Z. Ye, Y. Zhang, X. W. Fang, Z. J. Ding, C. Z. Wang, M. I. Mendelev, R. T. Ott, M. J. Kramer, and K. M. Ho, 'Crystal genes' in metallic liquids and glasses, Sci. Rep. **6**, 23734 (2016).

[64] O. Kubaschewski, *Iron-binary Phase Diagrams* (Springer Science & Business Media, New York, 2013).

[65] Y. Sun, Y. Zhang, F. Zhang, Z. Ye, Z. J. Ding, C. Z. Wang, and K. M. Ho, Cooling rate dependence of structural order in $Al_{90}Sm_{10}$ metallic glass, J. Appl. Phys. **120**, 015901 (2016).